Constructing three-dimensional porous Ni/Ni_3S_2 nano-interfaces for hydrogen evolution electrocatalysis under alkaline conditions

Yiming An, Bolong Huang,* Zilong Wang, Xia Long, Yongcai Qiu, Jue Hu, Dan Zhou, He Lin, Shihe Yang*

Supporting information

1. Experiment details:

1.1 chemicals: all chemical reagents used here were purchased from sigma-aldrich without further purification.

1.2 Synthesis of oxidized carbon cloth

The carbon cloth was modified by surface oxidation according to acid oxidation of graphite powders. Briefly, several pieces of 1×3 cm^2 carbon cloth were put into 70 mL concentrated sulfuric acid at room temperature with magnetic stirring. Then 1.5 g sodium nitrate, 9 g potassium permanganate were added in sequence under vigorous agitation, the temperature was controlled below 20 ℃, the mixture was maintained in 40 ℃ water bath for 30 min. Then, 140 mL distilled water was added and the solution was stirred for 15 min. 500 mL water was added followed by a slowly addition of 20 mL 30% H_2O_2. The carbon cloth was washed with 1:10 HCl solution and then water for several times for further use.

1.3 Synthesis of P-Ni/Ni_3S_2

$Ni(OH)_xS_y$ was hydrothermally deposited onto the surface of oxidized carbon cloth (OCC). Typically, a piece of 1×3 cm^2 OCC with 12 mL aqueous solution containing 0.125 M of $NiCl_2 \cdot 6H_2O$, 0.25 M of $C_6H_{12}N_4$ (HMT), and different concentration of thiourea (0.027 M, 0.045 M, 0.135 M) were placed into a 20 mL glass vessel. The vessel was sealed with plastic cover, and keep in 100 ℃ for 10 h. The $Ni(OH)_xS_y$ grown on OCC was washed with distilled water and ethanol, and dried in vacuum oven. One side with a thick layer of $Ni(OH)_xS_y$ was removed from OCC. Finally, the product was treated in H_2/N_2 mixed gas (5.0 vol%) at 400 ℃ for 1 h with heating rate of 5 ℃/min.

1.4 Synthesis of P-Ni

The procedure is the same as synthesis of P-Ni/Ni_3S_2 without addition of thiourea.

1.5 Synthesis of P-Ni_3S_2

$Ni(OH)_2$ grown on OCC was obtained using the same precursor solution as $Ni(OH)_xS_y$ without addition of thiourea. Then, the dried product with 40 mL ethanol solution containing 0.1125 g thioacetamide were put into the Teflon-lined stainless steel

autoclave, heated at 120 ℃ for 6 h. After washed with distilled water and ethanol, the sulfurized product was dried and then treated in H_2/N_2 mixed gas (5.0 vol%) at 400 ℃ for 1 h with heating rate of 5 ℃/min.

1.6 Synthesis of P-Ni/Ni_3S_2 sheets and Ni foam (NF) /Ni_3S_2

P-Ni on carbon cloth and a piece of cleaned NF were put into two 25mL Teflon-lined stainless autoclaves, 15mL 1.2 mM thiourea solution was then transferred into autoclaves respectively. The autoclaves were sealed and heated at 150 ℃ for 5 h. The products were then cleaned with distilled water and ethanol several times, and dried in vacuum.

1.7 Two step sufurization of $Ni(OH)_2$

$Ni(OH)_2$ grown on OCC was obtained using the same precursor solution as $Ni(OH)_xS_y$ without addition of thiourea. Then $Ni(OH)_2$/OCC was placed into a 20 mL glass vessel containing 12 mL 0.045 M thiourea aqueous solution. The vessel was sealed with plastic cover, and keep in 100 ℃ for 10 h. The $Ni(OH)_xS_y$ grown on OCC was washed with distilled water and ethanol, and dried in vacuum oven.

1.8 physicochemical characterizations

The morphology of the sample was analyzed using scanning electron microscopy (SEM, JSM-6700F). The composition and structure were characterized by X-ray diffraction (XRD, PW 1830, Philips), X-ray photoelectron spectroscopy (XPS, PHI 5600), transmission electron microscopy (TEM, JEM-2100F), and Brunar-Emmett-Teller (BET) surface areas and N_2 absorbing-desorbing isotherms (SA3100).

1.9 Loading mass determination

The weight of OCC substrate was measured and denoted as x_1 g. After synthesis of P-Ni/Ni_3S_2, the weight was noted as x_2 g. The loading mass equals to (x_2-x_1) g, which is about 1.4 mg.

1.10 Electrochemical characterizations

Electrochemical tests were carried out in standard three electrode system, CHI 760D electrochemistry workstation. Catalyst grown on OCC was directly used as working electrode, platinum wire as counter electrode, and Hg/HgO electrode as reference electrode. The reference was calibrated and converted to reversible hydrogen electrode (RHE).

Electrochemical double layer capacitances were measured to characterize the electrochemical surface area (ECSA) by cyclic voltammetry (CV) method. The current density was calculated using fixed geometric area of oxidized carbon cloth (OCC) substrate.

Linear sweep voltammetry (LSV) was obtained with scan rate of 5 mV/s for polarization curves. Before HER measurement, the electrodes were cycled about 5 times for electrochemical pretreatment until the cyclic voltammetry (CV) curve became stable. All polarization curves and durability test have been iR-corrected.

Chrompotentiometry (CP) was conducted under constant current density of 5 mA/cm^2

and 10 mA/cm^2.

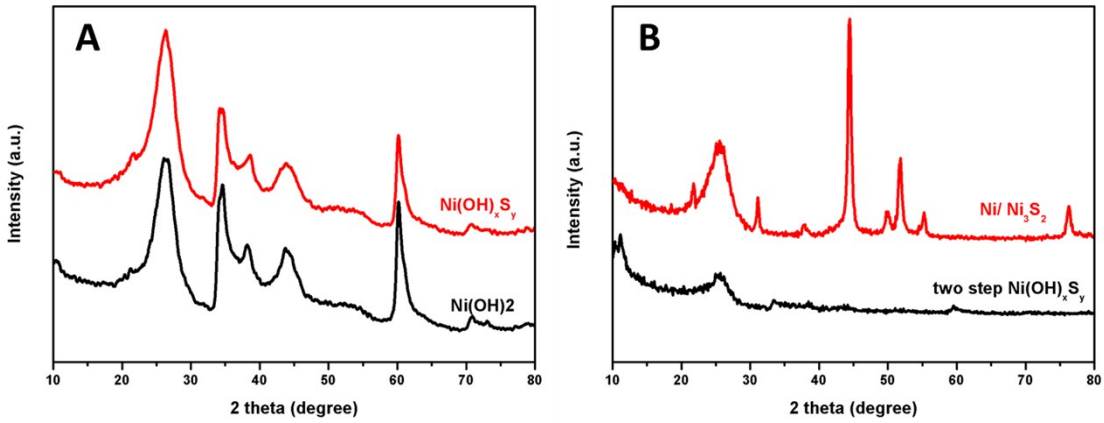

Figure S1. XRD image of A) $Ni(OH)_2$ and $Ni(OH)_xS_y$ nanosheet precursor on carbon cloth B) $Ni(OH)_xS_y$ by two step hydrothermal sulfurization (black curve) and Ni/Ni_3S_2 obtained by H_2 annealing of two-step sulfurized $Ni(OH)_xS_y$ (red curve). The resulting materials after H_2 annealing are Ni/Ni_3S_2 no matter the precursor is prepared by one-pot or two step sulfurization of $Ni(OH)_2$. The peak positions of two-step sulfurized $Ni(OH)_xS_y$ are the same with one-pot sulfurized $Ni(OH)_xS_y$, while it is relatively weaker because of the different degree of sulfurization. The same products indicate the ion exchange process happened at the $Ni(OH)_2$ surface when synthesizing $Ni(OH)_xS_y$ precursur by one-pot method.

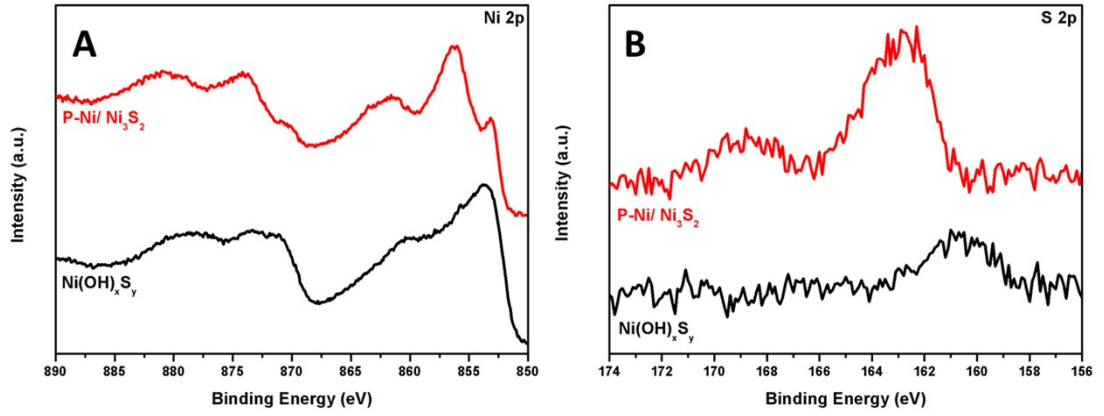

Figure S2. XPS spectra of A) Ni 2p peaks and B) S 2p peaks for $Ni(OH)_xS_y$ nanosheet precursor (black curve), and $P\text{-}Ni/Ni_3S_2$ (red curve). The element states of Ni and S in $Ni(OH)_xS_y$ are slightly different from which in $P\text{-}Ni/Ni_3S_2$. The Ni at $Ni(OH)_xS_y$ surface are mostly Ni^{2+}, and the S are in sulfide state instead of S $^{\delta-}$ in Ni_3S_2. The peaks of $P\text{-}Ni/Ni_3S_2$ including Ni 2p and S 2p show positive shifts compared with standard peak position, indicating the good combination between Ni and Ni_3S_2 which induced this shifts.

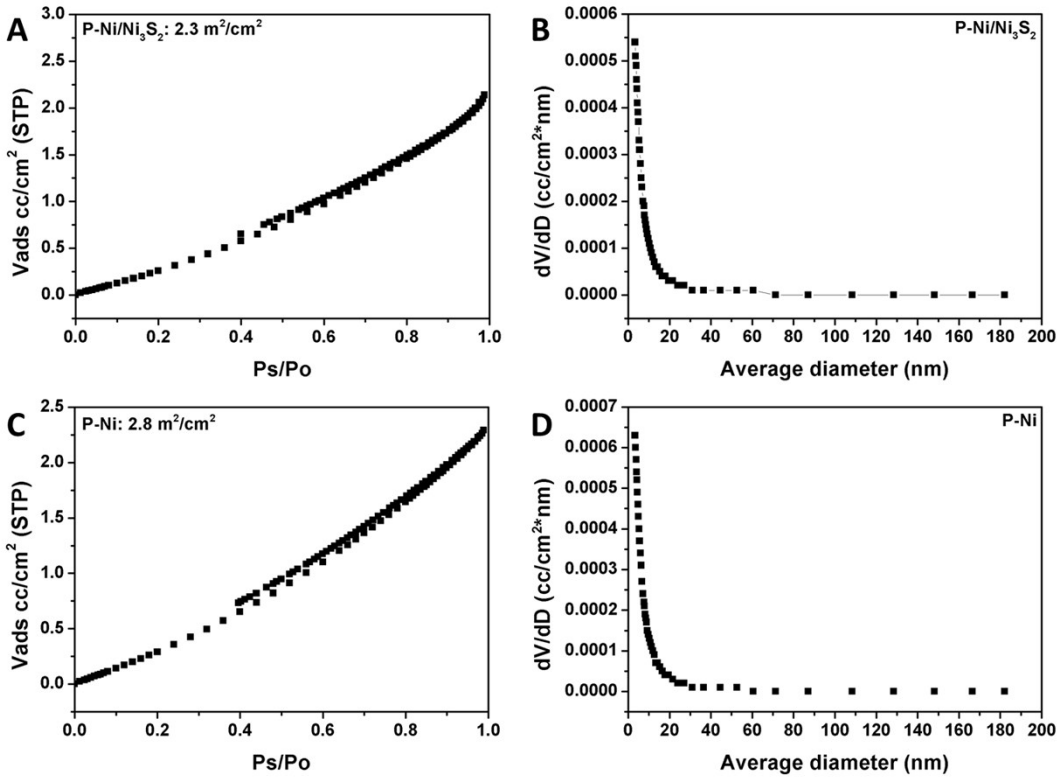

Figure S3. A) N_2 adsorbing-desorbing isotherm curve of P-Ni/Ni_3S_2 B) BJH pore size distribution curve of P-Ni/Ni_3S_2 C) N_2 adsorbing-desorbing isotherm curve of P-Ni D) BJH pore size distribution curve of P-Ni.

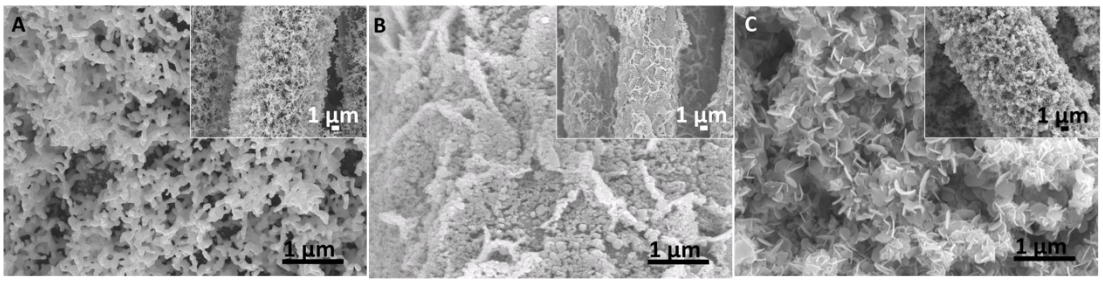

Figure S4. SEM images of A) P-Ni B) P-Ni_3S_2 C) P-Ni/Ni_3S_2 sheets.

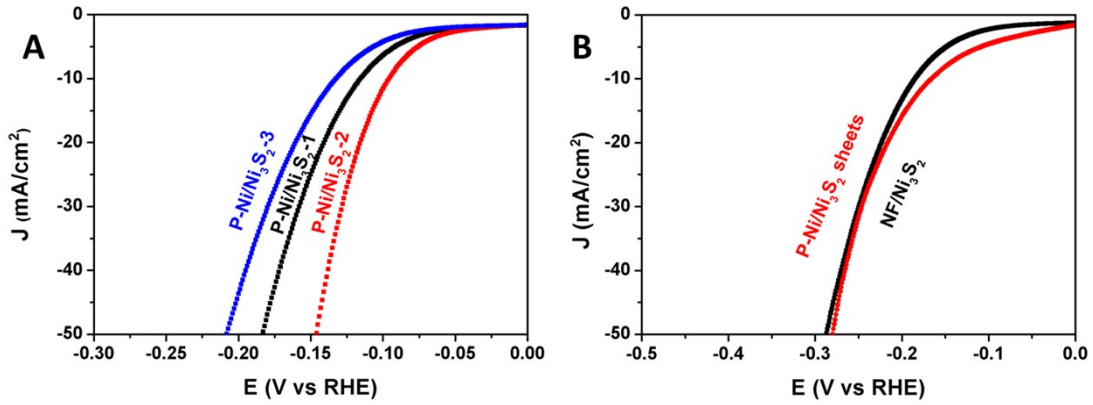

Figure S5. LSV curves of A) P-Ni/Ni_3S_2-1 (thiourea 0.027 M), P-Ni/Ni_3S_2-2 (thiourea 0.045 M), and P-Ni Ni_3S_2-3 (thiourea 0.135 M)

B) P-Ni/Ni_3S_2 sheets and NF/Ni_3S_2 in 1 M KOH.

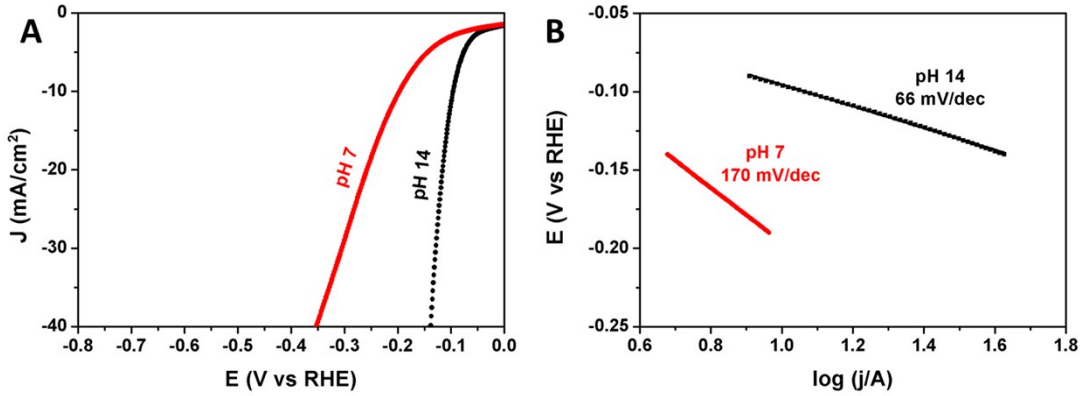

Figure S6. Electrochemical performances of P-Ni/Ni_3S_2 in electrolyte of different pH on HER. A) LSV curves, B) Tafel plots of P-Ni/Ni_3S_2 in phosphate buffer solution (pH≈7) and 1 M KOH (pH 14) solution

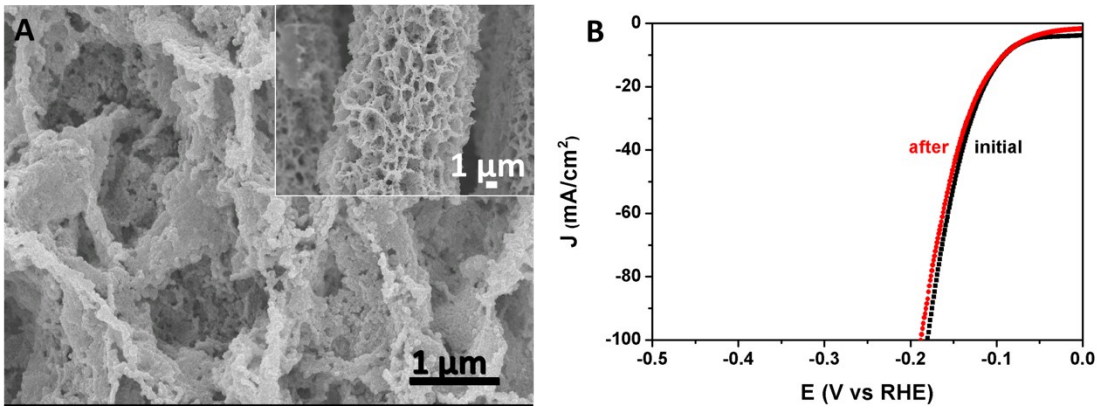

Figure S7. A) SEM images of P-Ni/Ni_3S_2 after 10h HER durability test B) LSV curve of P-Ni/Ni_3S_2 before and after HER CP testing at 10 mA/cm^2 for 10h. The performance of P-Ni/Ni_3S_2 before and after HER in 1 M KOH shows very small shift.

DFT calculation

1. Modeling of water splitting on pure Ni_3S_2 (111) surface

The excellent catalytic performance of Ni_3S_2 is closely related to the surface water splitting effect for applications of HER and OER. Such catalytic feature is usually determined by the surface reactivity of the solid nanomaterials. As recently discussed by Zhuang et al [1], the surface electronic density of states (DOSs) are the dominant factor that determines the charge transfers and energy conversion among the surface catalytic chemical reactions. Thus, it is necessary to start-up a theoretical study on electronic properties of Ni_3S_2, as well as a series of modeling of water splitting on Ni_3S_2 surface to our better understand the mechanism.

2. Bulk geometry and electronic properties

The bulk phase of Ni_3S_2 has a nearly cubic structure with symmetry of R32. In the lattice, the Ni has 4-fold coordinated local configuration, while the S is 6-fold coordinated. This shows slightly difference between conventional sulfides since they usually have S sites with a lower coordination than the sites of cation. This implies the charge transfer occurs more evidently on S site compared

with Ni. The geometry optimization based on our method shows the lattice parameter a=4.45 Å, with 9% larger than the reported 4.07 Å. This may arise from the d-orbital repulsive effect that applied by d-orbital on-site Coulomb energy correction by Hubbard-U parameter. The lattice optimized by Zou et al has closer data of 4.01 Å with 1.5 % shrinkage without semi-core 3d orbital on-site correction in plain GGA-PBE calculation [2]. Each Ni site has two long Ni-S bonds with length of 2.46 Å and two short Ni-S bonds with 2.42 Å in length, meanwhile, the distance of first nearest neighboring Ni site is 2.90 Å. The details of calculation setting-up and calculation method are provided in the supplemental materials.

We modeled Ni_3S_2 using the lattice within R32 space group, and the lattice relaxation of at the ground states is accomplished at the both PBE and PBE+U level by CASTEP code [3], since the PBE as the first Jacob ladder in DFT has been recognized to be reliable for structural relaxation and cell optimization of d- or even f-orbital based solids [4-6], independent to the choice of pseudopotentials. However, the electronic structures are the key dominant features that usually underestimated and significant to interpret the electronic and energy transfer process for HER mechanism. Thus, to improve the accuracy of the electronic structure calculations, the Hubbard U parameter has been induced in PBE+U calculations.

It is also found that the electronic states in the optical fundamental gap are less sensitive to the nonlinearity of Hubbard U parameters on the semicore d orbitals. Therefore, we choose Anisimov-type rotational-invariant DFT+U method [7], and the spin-orbital coupling effect here is simplified into very small magnitude. To minimize the effect of the localized hole states produced by 2p orbitals of O sites, the self-consistently determined Hubbard U potentials is also applied on the O-2p orbitals, which have been reached a consensus [8-11] in many oxides materials. Thus, it is necessary to consider both self-energy corrections on semicore orbitals for oxides [12-15]. However, the non-self-consistently determined Hubbard U parameters usually induce an error in lattices relaxation due to the non-zero residue of second-order partial derivative to the charge density. It is necessary to consider our established self-consistent determination of U parameter on the electronic structures [5, 11-16], in order to minimize the error on the lattice relaxation.

For describing the behavior of valence electrons, we chose the (3d, 4s) states as valence states of Ni, and (3s, 3p) for S, respectively. The OPIUM code in the Kleinman-Bylander form norm-conserving pseudopotential [17] with non-linear partial core correction[18] is chosen to minimize the systematic error due to the atomic core-valence electron densities overlap. Further the RRKJ method is selected to optimize the basis sets and ionic minimization of pseudopotentials[19]. The norm-conserving pseudopotentials is used because it can reproduce the all-electron behavior for outter shell valence electrons with |S-matrix|=1 compared to ultrasoft pseudopotentials[20, 21]. As all of the constituent elements (Ni and S) are light elements, the spin-orbit coupling effect has not implemented over the calculations. The kinetic cutoff energy of 750 eV, which expands the valence electrons states in a plane-wave basis set. To prevent the charge-spin out-sync sloshing effect and guarantee the electronic minimization and convergence, the ensemble DFT (EDFT) method of Marzari et al[22] is used for solving Kohn-Sham equation. The reciprocal space integration was performed by k-point sampling with grids of 5 × 5 × 4 k points in the Brillouin zone of hexagonal-unit-cell representation of Ni_3S_2 lattice, and 2 × 2 × 2 for defect electronic structures calculations in supercell respectively. We further select the (¼, ¼, ¼) special k-point[23] in the 2x2x2 supercell. This converges the total energy to under $5.0x10^{-7}$ eV per atom. The Hellmann-Feynman force on each atom was converged to lower than 0.01 eV/Å. The geometry optimization used the Broyden-

Fletcher-Goldfarb-Shannon (BFGS) algorithm through all bulk and defect supercell calculations. With our self-consistently determination process[5, 6, 12-15, 24, 25], the on-site Hubbard U parameters for 3d of Ni is 6.34 eV and 9.69 eV for the 3p of the S, respectively. The process is illustrated in the Figure S8 as follows, and they have also been compared with the pure Ni metal phase and pure S elemental states.

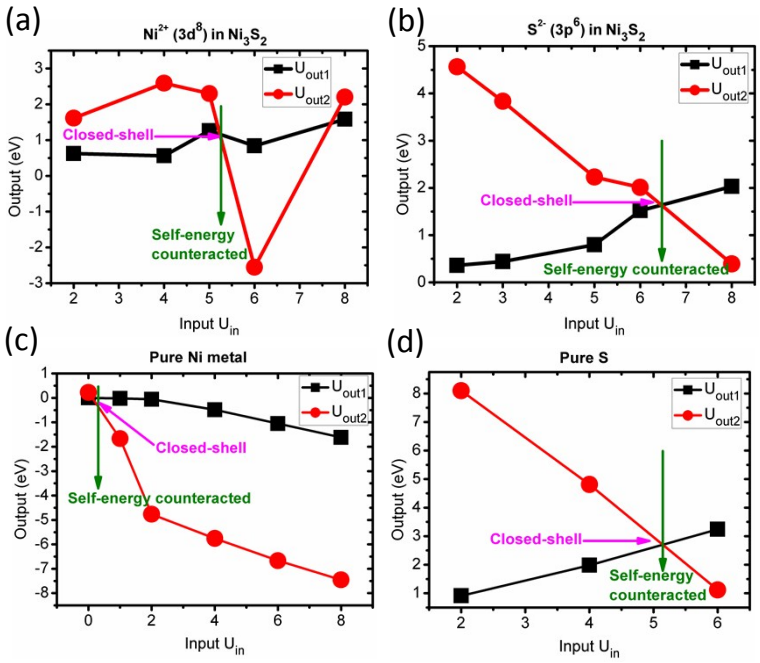

Figure S8. The Obtained Hubbard projections of a) U_{out1} and U_{out2} for 3d orbitals of Ni^{2+} and b) 3p orbitals of S^{2-} in Ni_3S_2 are shown and a comparison with c) pure Ni metal and d) S element states is given.

For the band structure and bulk DOSs, we show as following Figures S9 and S10. It is a conductor with crossover state at the Fermi level (EF, 0 eV). From the orbital projected DOSs (PDOSs) of Ni_3S_2, we see that there is a slight overlap of p-d orbitals near the EF. For the 3d orbitals, they contribute three distinguished peaks with spin-up across EF acting similarly as the HOMO level of bulk of Ni_3S_2. The empty states of 3p of S sites and 3d orbitals of Ni sites play as dominant components from conduction band (CB). Thus, the LUMO level is contributed by a state of 3p-3d overlap.

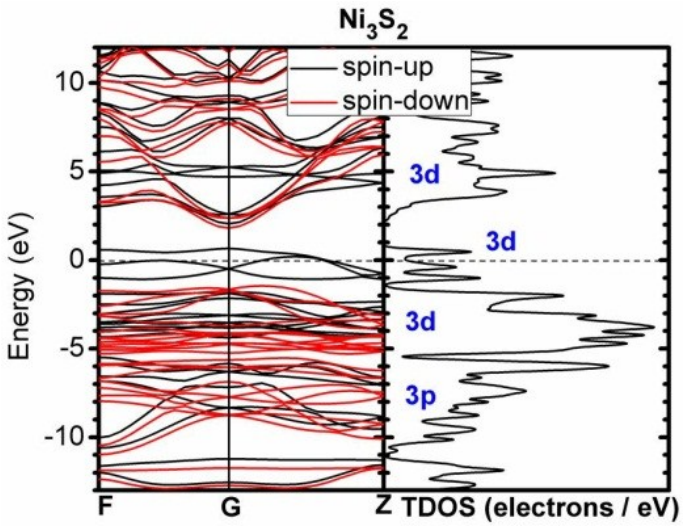

Figure S9. Band structure of bulk Ni_3S_2 by self-consistent PBE+U calculations, the U parameters are determined by our developed ab-initio method[15].

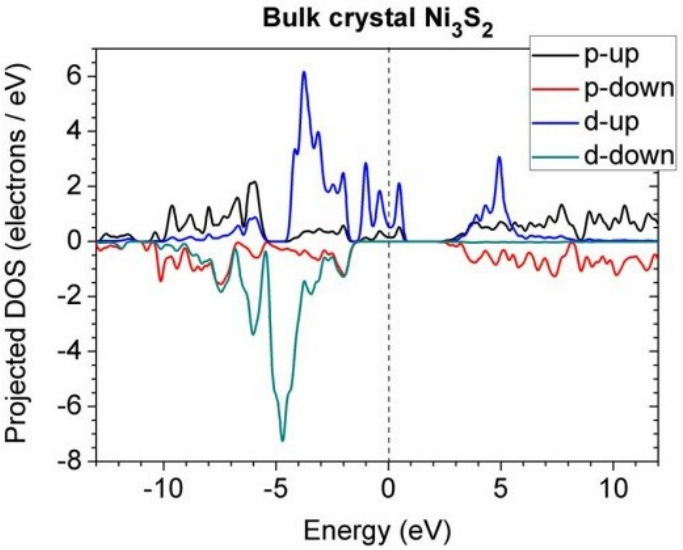

Figure S10. Projected density of states (PDOS) of bulk Ni_3S_2, based on the self-consistently calculated band structures.

Electronic property changes induced by the intrinsic S-vacancy

Here we introduce some finding that, the native electronic property in ideal Ni_3S_2 lattice is a conductor as confirmed in Figure S9 and S10. However, in nature realistic cases, the as-synthesized Ni_3S_2 particle samples cannot guarantee its perfection in both stoichiometric ratio and lattice arrangement etc. Therefore, we consider the probability of existence of S-deficit (i.e. S-vacancy, or VS) in the Ni_3S_2 lattice and its related impact on the change of electronic properties.

On the other hand, recent experiment by Prasad et al shows that the nanosized Ni_3S_2 samples present a semiconductor characters in electronic DOSs measured by CV [26]. The energy gap is then reported about 2.81 eV. Our calculated DOSs of Ni_3S_2 with S vacancy (VS) also shows a behavior like wide band gap semiconductor, with predicted band gap of 2.96 eV in Figure S11. Note that, this is not a real electronic fundamental band gap that usually discussed in the semiconductor solids. This is just an instability demonstrated between the components of e_g and t_{2g} of 3d orbitals

at Ni ions near the VS site. Moreover, this may be optical selection rule forbidden, because the d-d transition is restricted in some cases of symmetries.

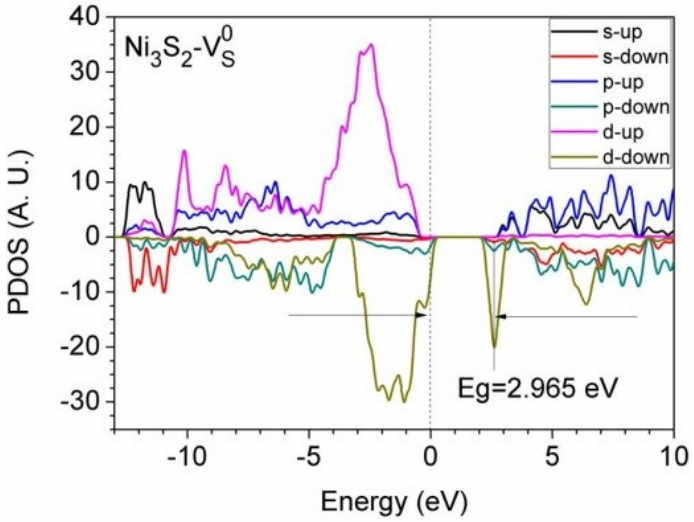

Figure S11. The calculated projected DOS (PDOS) of Ni_3S_2 with S-vacancy (VS) in the neutral state.

Then, why the spin-alignment is in the same configuration? We deduce that this arises because the electronic realignment on the 3d orbitals near EF at the VS site. The change in electronic properties induced by VS in the Ni_3S_2 lattice may be responsible for the experimentally measured band gap opening effect of the Ni_3S_2 system [26]. This is also reasonable since the synthesized Ni_3S_2 nanomaterial usually contains intrinsic defects such as vacancy. As the Figure S12 illustrated, the electrons left by VS are localized on the 3d orbitals of six nearby Ni-sites. The electron localization results in the splitting of bonding-antibonding orbitals which opens a forbidden electronic band gap. While the difference between defective and ideal lattice arises at the LUMO state that has mainly given by the 3d orbitals with spin-down. Similar effect has been also observed in the system with Peierls distortion. Under the S-rich chemical potential limit, we self-consistently estimate the formation energy of the VS in Ni_3S_2 with an energy cost of 1.84 eV. This shows a physicochemical trend that the formation energy in the S-poor would be even lower than the calculated value 1.84 eV, which indicates the probability of formation of VS in the Ni_3S_2 lattice is very high in real case.

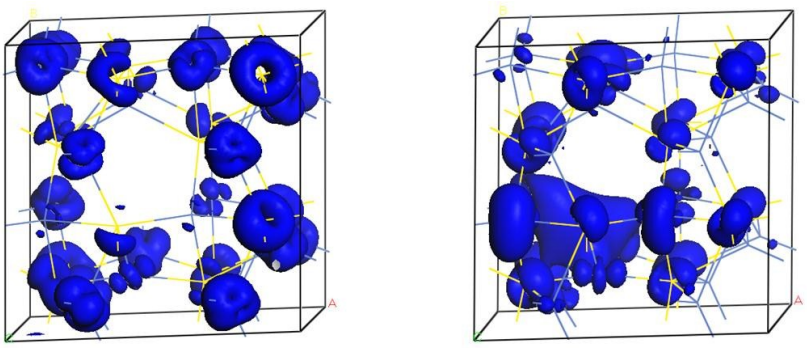

Figure S12. The calculated 3D real-space HOMO (left) and LUMO (right) localized states of Ni_3S_2 supercell lattice with one VS.

Energy evolution process for the H_2O splitting

The H_2O splitting on the (111) surface of Ni_3S_2 has been modeled to elucidate how the local energy competitions of Ni-O, S-H, and Ni-H bonds from the short to medium ranged order. Ni_3S_2 (111) has many distorted honeycomb hexagonal ring with Ni and S numbers are 3: 3 respectively. The following Figure S13 has been illustrated the typical transition steps of the H_2O at the different locations of Ni_3S_2 (111) system in terms of surface total energies. We take the absorption of H_2O at the hollow site as the first step and its total surface energy is treated as zero reference energy (0 eV). In this step, the structural configuration shows that the O from H_2O is sharing with neighboring Ni sites. Figure S14 interprets the process how the H_2O energetically favorably split on the Ni_3S_2 (111) surface. As suggested by our preliminary molecular dynamics, we model that the H_2O would rotate 90° for better overlap of p-π and dz (step 2), and will then approach to the middle line of Ni-Ni long bonds on (111) system (step 3-4). But this rotation of H_2O on (111) lead to the total energy of surface system increased as high as 0.68 eV.

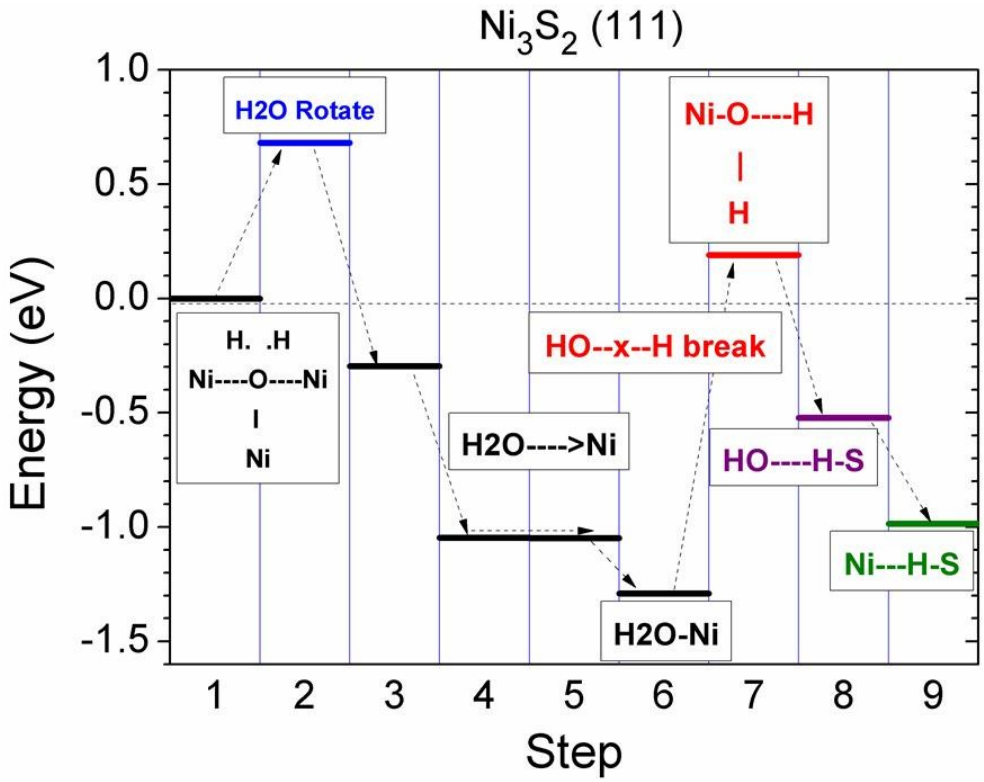

Figure S13. Transition energy levels of one single H_2O splitting evolution process on Ni_3S_2 (111) system.

Accordingly, it seems that there is an energy barrier for H_2O rotating on Ni_3S_2 (111) in order to reach a better p-d bonding overlap. However, this shows an evident down trend of total energy for the (111) system at the step 3 and 4, which is from -0.30 eV to -1.05 eV. This indicates an energetic preference of O in H_2O to form a coupling with two Ni sites of that distorted honeycomb unit where three Ni form a triangle shape. We intend to illustrate how the process of breaking O-H and bonds to Ni (weak O-Ni coupling). Thus, the next scenario for H_2O is a further approach or contact to one of these two Ni sites (step 5). It seems a flat energy surface for H_2O oscillates nearby the two Ni-Ni middle line, as the energy difference of step 5 has only 3 meV compared with the structural configuration of step 4.

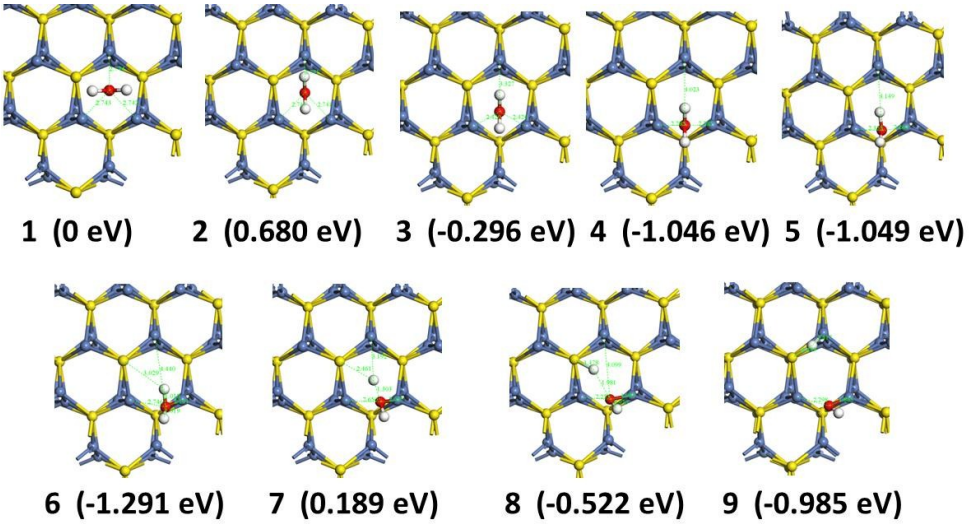

Figure S14. The steps of H_2O splitting on Ni_3S_2 (111) system corresponding to the transition energy levels shown in Figure S13.

We found that the lowest energetic configuration for H_2O is to bond with one of the Ni site with pdσ as a strong bond, and the energy gives -1.29 eV in magnitude. (step 6). Therefore, step 1-6 show an evolution process that how one H2O molecule is captured and located. How is the energy evolution when breaks an O-H bond? Step 7 in Figure S14 shows that the estimated energy for this modeling configuration is 0.19 eV. It means a potential barrier exists in the process that captures H_2O and breaks one of its O-H bonds, which is about 1.29 + 0.19 = 1.48 eV based on step 1-7 according to our calculation. This is consistent with experimental summarized 1.23 eV as potential energy to splitting H_2O for HER. Such itinerant H will be either captured by S or Ni site as the p-s and d-s overlap are both energetically favorable. Through compared the total energy of system at step 8 and 9, the energy is -0.522 eV and -0.985 eV, respectively. Hence we found the H will prefer the middle “bridge-bonding” with both nearby S and Ni sites. The remaining hydroxyl (OH) will stably stay at the Ni site with a strong pdσ interaction of O-Ni.

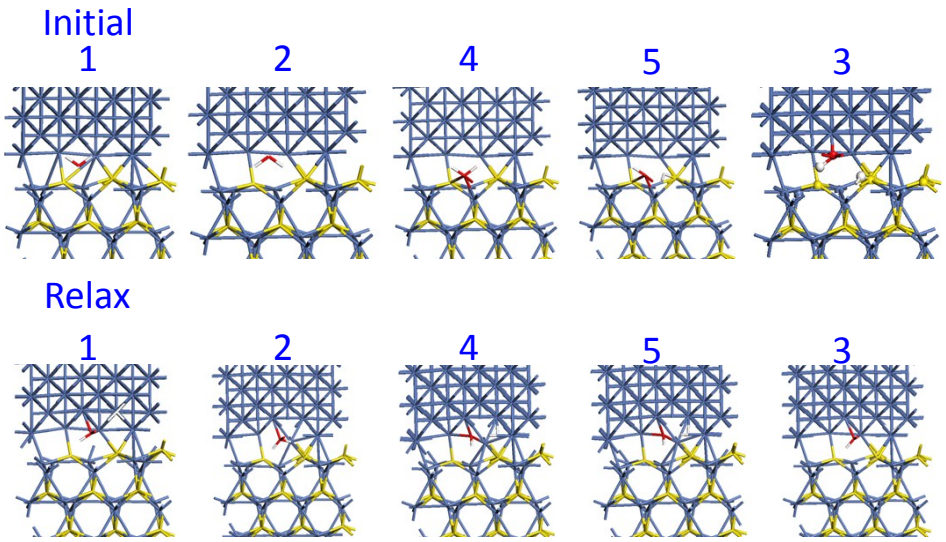

Figure S15. The steps of H2O splitting between Ni- Ni3S2 (111) interface region corresponding to the transition energy levels shown in Figure 9.

We further analyze the PDOSs of the interface system and the projected 3d orbital components in Figure S16. It is evidently shown that the EF is dominantly controlled by the 3d-orbitals of Ni seen from Figure S16 (a). As we discussed above in Figure S13 and S14 that, the Ni_3S_2 (111) are active in splitting H_2O into OH and H parts. However, the detail bonding on the surface usually produces some energy barrier for activating the splitting reaction. Moreover, the H after splitting is usually bonded with S site form a strong H-S bond which is less active in produce itinerant H atom to combine another for H_2 production (i.e. HER process).

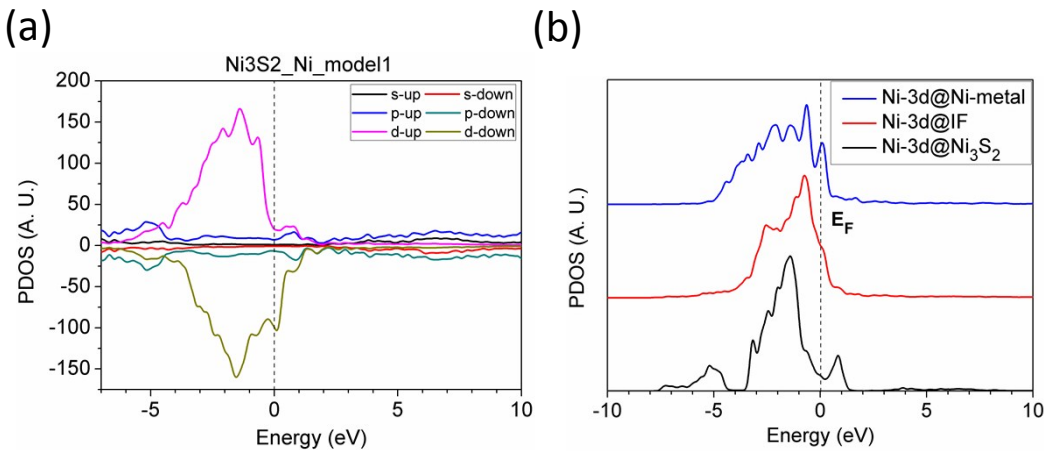

Figure S16. PDOSs of a) the interface and b) the projected 3d orbital components of different Ni sites from Ni_3S_2 (111), interface and Ni-metal parts are respectively shown.

Accordingly, we deduce that, it is the 3d occupied levels of Ni sites on the pure Ni_3S_2 (111) surface lying too high led to the over-binding to the H^+ (proton) on the surface. Now the interface changes the orbital levels by pushing the deep 3d orbital levels of Ni-site from pure Ni_3S_2 to a higher level that closed to the EF as shown in Figure S16 (b). The Ni-3d @ Ni_3S_2 denotes the pristine 3d orbital level of Ni site from the pure Ni_3S_2 (111) surface, staying at about 1.8 eV below the EF level. The Ni-3d orbital level at Ni-metal (Ni-3d@Ni-metal) is found to be pinned at the EF level. The Ni-3d level at the interface is different and giving a smooth transition from the Ni_3S_2 surface to the deep in the bulk of the Ni-metal. The related occupied level is staying at about 0.8 eV below the EF level with 1 eV shifted towards the EF. Therefore, the Ni-site at the interface region is playing as an assistant role that promoting the 3d orbital levels from the deep to a higher level close to the EF, and reducing the energy barrier of the 3d inter-orbital transition with about 1 eV in magnitude.

References

[1] B. Huang, L. Xiao, J. Lu, and L. Zhuang, Angew. Chem. Int. Ed. **55**, 6239 (2016).

[2] L.-L. Feng, G. Yu, Y. Wu, G.-D. Li, H. Li, Y. Sun, T. Asefa, W. Chen, and X. Zou, J. Am. Chem. Soc. **137**, 14023 (2015).

[3] S. J. Clark, M. D. Segall, C. J. Pickard, P. J. Hasnip, M. I. J. Probert, K. Refson, and M. C. Payne, Zeitschrift Fur Kristallographie **220**, 567 (2005).

[4] C. J. Pickard, B. Winkler, R. K. Chen, M. C. Payne, M. H. Lee, J. S. Lin, J. A. White, V. Milman, and D. Vanderbilt, Phys. Rev. Lett. **85**, 5122 (2000).

[5] B. Huang, Solid State Commun. **230**, 49 (2016).
[6] B. Huang, Solid State Commun. **237–238**, 34 (2016).
[7] I. A. Vladimir, F. Aryasetiawan, and A. I. Lichtenstein, J. Phys. Condens. Matter **9**, 767 (1997).
[8] S. Lany and A. Zunger, Phys. Rev. B **80**, 085202 (2009).
[9] S. Lany and A. Zunger, Phys. Rev. B **81**, 205209 (2010).
[10] B. J. Morgan and G. W. Watson, J. Phys. Chem. C **114**, 2321 (2010).
[11] P. R. L. Keating, D. O. Scanlon, B. J. Morgan, N. M. Galea, and G. W. Watson, J. Phys. Chem. C **116**, 2443 (2011).
[12] B. Huang, R. Gillen, and J. Robertson, J. Phys. Chem. C **118**, 24248 (2014).
[13] B. Huang, Philosophical Magazine **94**, 3052 (2014).
[14] B. Huang, J. Comput. Chem. **37**, 825 (2016).
[15] B. Huang, Phys. Chem. Chem. Phys. **Accepted**, DOI: 10.1039/C7CP00025A (2017).
[16] T. Zacherle, A. Schriever, R. A. De Souza, and M. Martin, Phys. Rev. B **87**, 134104 (2013).
[17] L. Kleinman and D. M. Bylander, Phys. Rev. Lett. **48**, 1425 (1982).
[18] S. G. Louie, S. Froyen, and M. L. Cohen, Phys. Rev. B **26**, 1738 (1982).
[19] A. M. Rappe, K. M. Rabe, E. Kaxiras, and J. D. Joannopoulos, Phys. Rev. B **41**, 1227 (1990).
[20] P. J. Hasnip and C. J. Pickard, Comput. Phys. Commun. **174**, 24 (2006).
[21] K. Laasonen, A. Pasquarello, R. Car, C. Lee, and D. Vanderbilt, Phys. Rev. B **47**, 10142 (1993).
[22] N. Marzari, D. Vanderbilt, and M. C. Payne, Phys. Rev. Lett. **79**, 1337 (1997).
[23] M. I. J. Probert and M. C. Payne, Phys. Rev. B **67**, 075204 (2003).
[24] B. Huang, Phys. Chem. Chem. Phys. **18**, 13564 (2016).
[25] B. Huang, Inorg. Chem. **54**, 11423 (2015).
[26] B. Busupalli, K. Date, S. Datar, and B. L. V. Prasad, Crystal Growth & Design **15**, 2584 (2015).
[27] K.-Y. Tse and J. Robertson, Phys. Rev. Lett. **99**, 086805 (2007).